Optically-ambidextrous circularly-polarized reflection from the chiral cuticle of the scarab beetle *Chrysina resplendens*

Ewan D. Finlayson, Luke T. McDonald and Pete Vukusic
Department of Physics and Astronomy, University of Exeter, EX4 4QL, United Kingdom

Accepted version (postprint).

Reference and link to final published version: Finlayson ED, McDonald LT, Vukusic P. 2017 Optically ambidextrous circularly polarized reflection from the chiral cuticle of the scarab beetle *Chrysina resplendens*. *J. R. Soc. Interface* 14: 20170129. http://dx.doi.org/10.1098/rsif.2017.0129

http://rsif.royalsocietypublishing.org

Corresponding author
Ewan D. Finlayson
E.Finlayson@exeter.ac.uk

Keywords
biophotonics
helicoidal self-assembly
structural colour
chirality

Electronic supplementary material is available online at https://dx.doi.org/10.6084/m9.figshare.c.3789964.

Abstract
The evolution of structural colour mechanisms in biological systems has given rise to many interesting optical effects in animals and plants. The instance of the scarab beetle *Chrysina resplendens* is particularly distinctive. Its exoskeleton has a bright, golden appearance and reflects both right-handed and left-handed circularly-polarized light concurrently. The chiral nanostructure responsible for these properties is a helicoid, in which birefringent dielectric planes are assembled with an incremental rotation. This study correlates details of the beetle's circularly-polarized reflectance spectra directly with physical aspects of its structural morphology. Electron micrography is used to identify and measure the physical dimensions of the key constituent components. These include a chiral multilayer configuration comprising two chirped, left-handed helicoids that are separated by a birefringent retarder. A scattering matrix technique is used to simulate the system's optical behaviour in which the roles of each component of the morphological substructure are elucidated by calculation of the fields throughout its depth.

1. Introduction

The varied and often spectacular appearance found among scarab beetles is accompanied in many cases by the property that the cuticle reflects circularly-polarized (CP) light (1-5). This attribute is particularly associated with certain species of jewel scarab of the genus *Chrysina* (formerly *Plusiotis*) that can also exhibit a brilliant metallic appearance. In 1911, the observation of the reflection of CP light by *Chrysina resplendens* (figure 1*a*) (6) was reported by Michelson (7). The cuticle structures responsible for this CP reflectance have been identified as helicoids (8, 9) that comprise birefringent planes of aligned chitin microfibrils embedded in a protein matrix, in which the azimuthal orientation of the microfibrils is rotated incrementally through successive stacked planes (figure 1*b*) (10). Helicoids may be identified in electron micrographs by a repeating lamellar arrangement of "Bouligand curves" (11) that appear in oblique sections (figures 1*c*, 1*d*). The helicoidal pitch is defined as the length over which the azimuth rotates through 360°, which comprises two lamellae. For normal incidence, CP light with the same handedness as the chiral structure is reflected in a spectral band that has a peak wavelength given by the product of the helicoidal pitch and the mean in-plane refractive index (8). The CP handedness is preserved upon reflection, in stark contrast to the action of a plane mirror, which reverses the CP handedness upon reflection due to the mirror inversion. The opposite-handed CP light is transmitted by the helicoidal medium. Helicoids are not limited to chitin-based systems; they are found in diverse natural structures (12-19) and are also identified with liquid crystals of the cholesteric phase (2, 9, 20). The ecological role of CP reflectance has been found to include CP signalling in mantis shrimps (21), requiring the visual discrimination of CP using complex photoreceptor structures in the compound eye (22).

While most species of *Chrysina* reflect only left-hand CP (LHCP) (1,23), *C. resplendens* is remarkable in that it also preserves right-hand CP (RHCP) upon reflection. The beetle may therefore be described as optically ambidextrous, which we define as having the ability to reflect both hands of CP. Caveney (8) characterised the structure experimentally and found that the birefringence is enhanced by the presence of uric acid. Two left-handed helicoidal regions were identified, separated by a "unidirectional layer" of birefringent material in which the rotation of microfibril planes is interrupted (figures 1*e*, 1*f*). This layer forms a birefringent retarder that is analogous to the nematic liquid crystal phase and acts as a half-wave plate within the reflectance band. The RHCP reflectance was thus explained by a switch to LHCP on transmission through the unidirectional layer, followed by reflection by the second helicoid and a switch back to RHCP on the return pass through the retarder. Both helicoidal regions were found to be chirped, whereby the smoothly-varying helicoidal pitch includes a range of dimensions, giving rise to broadband reflectance and therefore the appearance of a golden colour.

Further studies of the optical properties of *C. resplendens* have been reported. Goldstein (24) measured the wavelength-dependent Mueller matrix at normal incidence. Fernández del Río (25) conducted Mueller matrix spectroscopic ellipsometry including the dependence on the angle of incidence. Hegedüs *et al*. (26) undertook imaging polarimetry of a whole specimen at red, green and blue wavelengths. Hodgkinson *et al*. (27) recorded the Mueller matrix and additionally modelled the structure, applying Caveney's quantitative structural analysis. The model was found to provide a qualitative agreement with the measurements, matching "features rather than detail". Several applications inspired by the structure of *C. resplendens* have been described (28-30). In this work, we pursue a new level of detail in the correlation between the morphological configuration and the CP reflectance of this remarkable species.

2. Methods

2.1. Beetle specimen

The single preserved specimen of *C. resplendens* originated in Heredia Province, Costa Rica. All micrographic analyses and optical experiments were performed on cuticle taken from a centrally-located region of the left elytron.

2.2. Micrographic characterisation

In preparation for transmission electron micrography (TEM), samples were first fixed in 3% gluteraldehyde at 21°C for 2 hours, then rinsed in sodium cacodylate buffer. Subsequent fixing in 1% osmic acid in buffer for 1 hour preceded block staining in 2% aqueous uranyl acetate for 1 hour, dehydration through an ethanol series (ending with 100% ethanol), and embedding in Spurr resin. Following ultra-microtoming, the elytron sections were stained with lead citrate and examined using a JEOL JEM 1400 TEM instrument. Helicoidal pitch measurements were made by the identification of Bouligand features on groups of three lamellae, so that each measurement represents the mean length of three adjacent periods. Scanning electron micrography (SEM) was performed on fractured normal sections of cuticle using an FEI Nova 600 NanoLab machine. The sections were sputter-coated with a layer of AuPd prior to imaging. Further information is provided in the electronic supplementary material.

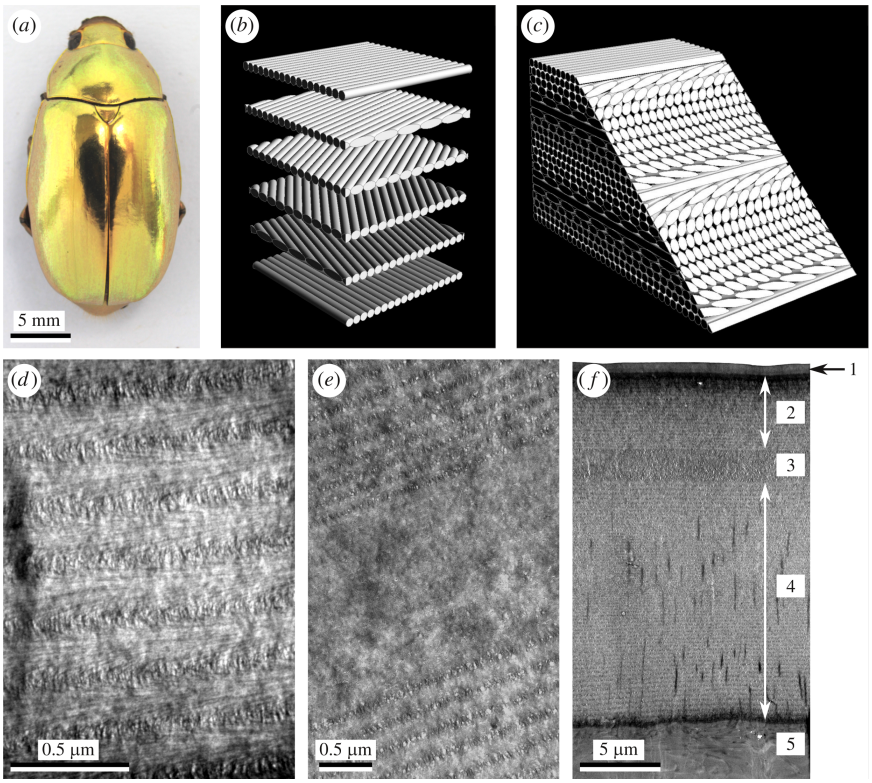

Figure 1. Helicoidal constructions and their exhibition in the scarab beetle *Chrysina resplendens*. (*a*) Dorsal view of *C. resplendens* photographed under unpolarized illumination. (*b*) An exploded view of a helicoidal set of filament planes. A left-handed helicoid is shown, in which successive planes farther from the observer are rotated anticlockwise. (*c*) A view of a section of an assembled helicoidal stack. The oblique cut reveals Bouligand curves in the filament arrangement. A full helicoidal pitch is shown, comprising two lamellae as indicated by the Bouligand curves. (*d*) TEM showing detail of an oblique section of the elytron of *C. resplendens*. Helicoidal lamellae are identified by the Bouligand curves. (*e*) TEM showing detail of a normal section of the cuticle. The unidirectional layer or birefringent retarder is shown as the uniform band extending across the centre of the image. Helicoidal regions are disposed above and below. (*f*) TEM of a normal section through the outer part of the cuticle of *C. resplendens*, indicating its component regions: 1: epicuticle; 2: upper helicoid; 3: unidirectional layer; 4: lower helicoid; 5: endocuticle (portion). Regions 2 to 4 form the exocuticle.

2.3. Optical reflectance measurements

The experimental setup for measurements of circular polarization reflectance is shown schematically in the electronic supplementary material (figure S4). The setup used a broadband fibre-coupled source (Ocean Optics HPX-2000) and a fibre-coupled spectrometer (Ocean Optics USB2000+). CP was generated by a rotatable polarizer followed by an achromatic Fresnel rhomb quarter-wave retarder orientated at 45° azimuth. The CP handedness was selected by setting the polarizer azimuth to either 0° or 90°. The incident light was focused onto the sample at normal incidence with a spot diameter of ≈30 µm by an achromatic ×10 microscope objective lens, which also collected the reflected light. The return beam was directed through a CP analyser comprising the Fresnel rhomb and a second rotatable polarizer via a beamsplitter. The system was calibrated using a plane mirror.

2.4. Optical modelling

The CP reflectance of the cuticle was modelled using a 4×4 matrix method for 1-D anisotropic multilayers (31-33), which was implemented with the scattering matrix modification of Ko & Sambles (34). The chirped helicoid was modelled using a spline interpolation fit to the measured lamellar pitch data, with sixteen sublayers per helicoidal period. Incoherent averaging (27) was used to reduce spectral modulation. Simulations of the fields within the structure were obtained from the forward and backward-propagating modal field amplitudes, which were extracted using the method detailed in (34). The CP content of the fields was analysed by the application of a Jones matrix for a circular polarizer of each selected hand.

3. Structural configuration

The main layers of the cuticle of *C. resplendens* may be summarised with reference to the TEM of its cross-section, shown in figure 1*f*, as comprising the outermost epicuticle, the exocuticle and the endocuticle layers (35-37). In *C. resplendens*, the exocuticle contains the helicoidal structures that are principally responsible for its distinct optical signature (8). In order to inform simulations of the optical behaviour of *C. resplendens*, the helicoid dimensions of the beetle specimen were quantified using electron micrography. SEM measurements of fractured normal sections of elytron yielded a value for the total exocuticle plus epicuticle thickness of 21.7 µm ± 1.8 µm (mean ± 1σ). Detailed measurements of the lamellar pitch variation and birefringent retarder thickness were made by TEM, which was performed on normal sections ultramicrotomed through the elytron (38). A sample of six separate

locations from the central region of the elytron was analysed in this way. The sum of layer thicknesses measured by TEM indicated a total exocuticle plus epicuticle thickness of 19.7 µm ± 0.8 µm. Several factors may contribute to the discrepancy between these SEM and TEM measurements. Uncertainties in the TEM length measurements may arise due to the possibilities of artefacts such as shrinkage or compression (39) of the microtomed sections and measurement tolerances. Neville & Caveney (9) estimated shrinkage of 6.1% to 10.7% in microtomed beetle exocuticle. Moreover, the larger sample of 89 independent locations quantified by SEM provides a more representative data set.

The measurements of the beetle's elytral lamellar pitch are shown in figure 2, as well as a fit curve. In five of the six TEM measurement locations the total number of lamellae identified varied between 98 and 102, comprising either 20 or 21 complete lamellae in the upper helicoid and between 78 and 81 in the lower helicoid. In the sixth region only 90 complete lamellae were found, 71 of which were in the lower helicoid. The upper helicoid is shown to be chirped, with the lamellar pitch diminishing from typically 210 nm at the distal limit to around 145 nm at the proximal limit. Interestingly, the lower helicoid has an elaborate pitch variation containing several reversals of the sign of the chirp and a broad range of pitch dimensions, for which the fit-curve spans 115 nm to 260 nm. The mean thickness measured for the unidirectional layer was 1.60 µm. The uppermost observed layer was identified as the epicuticle by the absence of Bouligand structures, with an approximate thickness of 0.6 µm. In defining a representative model of the structure for use in simulations, the lamellar pitch values were scaled by the factor 1.1 in order to match the total exocuticle thickness to the mean SEM measurement. These scaled data, in conjunction with selected refractive index data, were found to permit a closer match between simulations and spectral measurements. The scaled fit curve is also shown in figure 2. Accordingly, the unidirectional layer was modelled with a thickness of 1.76 µm.

Several authors have written of the lack of accurate complex refractive index data for natural chitin-based structures (40-42) and of the differences in the specific composition that are found due to the inclusion of proteins and other compounds (8, 43). Measurement is not straightforward, particularly in beetle elytra, due to surface curvature, scattering and non-uniformity (42). Noyes *et al*. (41) discussed the refractive indices reported for various species, which covered the range 1.4 to 2.0. More recently, Yoshioka *et al*. (42) obtained complex refractive indices including wavelength dispersion for electron-dense and electron-lucent layers of the jewel beetle *Chrysochroa fulgidissima*. Leertouwer *et al*. (44) obtained the wavelength-dependent index for the chitinous wing scales of the butterfly *Graphium sarpedon*, and noted a negligible imaginary part for this unpigmented system. Caveney's refractive index measurements on *C. resplendens* were made by direct studies of the unidirectional layer at the single wavelength of 560 nm, and yielded the values 1.535 and 1.701 in the plane parallel to the cuticle surface. The specific composition of the exocuticle was found to include a uric acid fraction of 0.7, and the role of that compound in enhancing the birefringence was established.

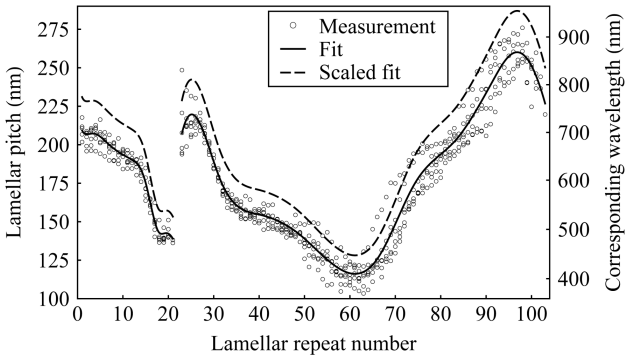

Figure 2. Lamellar pitch values (circles) measured from micrographs of normal sections of the cuticle of *C. resplendens*, fit curve (solid line) and scaled fit (dashed line) used in the simulations. The break in the data after lamellar repeat number 21 indicates the position of the birefringent retarder that separates two left-handed helicoids. One helicoidal period comprises two lamellar periods.

In selecting the refractive index data for use in simulations of the system, the importance of uric acid is taken into consideration. For the spatial average of the real part of the refractive index of the helicoidal and unidirectional layers we adopt the values for chitin and uric acid published by Vargas *et al*. (45). These data have been applied in simulations of *C. aurigans* (46). An effective medium approximation (47) is applied with a uric acid fraction of 0.7. A least-squares fit to the data yields the Sellmeier equation (wavelengths in µm):

$$\bar{n}^2 = 1 + \frac{1.62\,\lambda^2}{\lambda^2 - 0.0289}\,. \qquad [1]$$

We estimate the in-plane wavelength-dependent birefringence from reflectance measurements performed on the reflecting structure. The different responses obtained for incidence upon the dorsal surface and incidence upon the exposed surface of the underside of the elytral exocuticle yield information about the retardation imparted by the unidirectional layer. This measurement is discussed further in the results section. While this method only affords an inference of the birefringence, it benefits from a relative lack of intervention in preparing the sample for measurement, in comparison to microtomy for example.

The beetle epicuticle is composed of non-chitinous sclerotised lipids and proteins and typically comprises outer and inner epicuticle regions (36), with the latter forming the larger part of the layer. Weis-Fogh (35) reported an isotropic refractive index of 1.58 for this material in *Schistocerca* locusts, and we adopt this value for the entire epicuticle. Thin layers of cuticular wax and cement (36, 37) that coat the epicuticle are not distinguished in our model. Reported values for the extinction coefficient of reflective chitinous material range over several orders of magnitude, from ~10^{-4} to ~10^{-1} (41, 42, 45), where the larger values are typically associated with the presence of melanin (48, 49). The arbitrary value 0.0012 is found to permit a representative match between our model and the experimental data, and is applied throughout the structure for all wavelengths. This value is comparable to examples reported for melanin-free insect cuticle (50) and coleopteran cuticle (42).

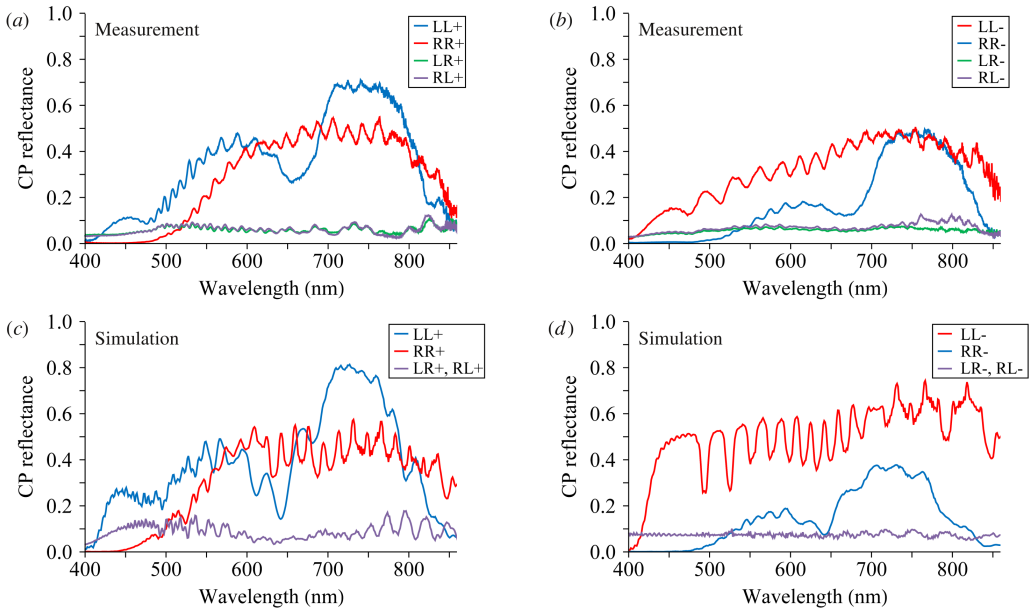

Figure 3. Experimental measurements and simulations of the circular polarization absolute reflectance of the elytral cuticle of *C. resplendens* at normal incidence. The CP components are denoted by two letters indicating (first) the incidence and (second) analyser CP hands, while + and – represent incidence upon the dorsal surface and the exposed exocuticle underside surface respectively. In each plot, the blue and red curves indicate the CP component that is attributed principally to the upper and lower helicoids respectively. (*a*) Experimental result, incidence upon dorsal surface; (*b*) Experimental result, incidence upon the prepared exocuticle underside surface following removal of the endocuticle; (*c*) Simulation, incidence upon dorsal surface; (*d*) Simulation, incidence upon exocuticle underside surface.

In addition to the observed variation of the structure within the specimen, differences between specimens are to be expected. The lamellar dimensions and features of our specimen are broadly comparable to those measured by Caveney, with a notable exception in the upper helicoid. While both specimens show a similar distribution of helicoidal pitch values, they are chirped with opposite gradients. This discrepancy is demonstrated by the clear difference in the helicoidal pitch on either side of the birefringent retarder that may be seen in the micrograph of figure 1*e*, while a similar image in (8) shows no such difference. Fernández del Río (25) noted that four specimens of *C. resplendens* showed differences in the measured m_{41} Mueller matrix parameter, suggesting differences in their structures. Hegedüs *et al.* (26) found differences between measurements of the polarization response of the dorsal and ventral surfaces, and the legs.

4. Results and discussion

CP-specific reflectance measurements were performed on the cuticle with the independent selection of each hand of circular polarization for incidence and for reflectance analysis. All four CP combinations were measured. In addition to the measurements of the reflectance of the dorsal surface of the cuticle, a piece of the elytron was prepared to enable optical reflectance measurements to be performed with incidence upon the underside of the lower helicoid. The soft endocuticle, including a pigmented layer, was removed mechanically to expose an area of the hard exocuticle, which was identified by its reflective appearance. The reflectance was modelled using a scattering matrix method (31-34), using the structural parameters described above. In the following discussion, we use the term “dorsal surface” to refer to the elytral epicuticular surface, and “exocuticle underside” to refer to the lower helicoid surface of the elytron, i.e. the exposed ventral surface of the elytral exocuticle.

The measured and simulated CP reflectances for LHCP and RHCP incident fields at normal incidence are shown in figure 3. The two cases of incidence upon the dorsal surface and the exposed underside of the exocuticle of the elytron are compared. The CP reflectance components are distinguished by notation of the form LR+ for example, in which the first and second letters indicate the incidence and analyser CP hands respectively, while + and – represent incidence upon the dorsal surface and the exposed exocuticle underside respectively. Figure 3*a* shows a typical experimental result for incidence on the dorsal surface of the elytron. The LL+ and RR+ spectra for a further sample of eighty positions on the central part of the elytron (see electronic supplementary material, figure S1) show that the main features of the CP spectra were consistently present across the sample of locations, and that some variation in the relative intensities and spectral positions of the features was observed. Reduced reflectance was found at some sites, which may be attributed to the coincidence of the illumination with cracks, pores or localised corrugation of the surface.

We now consider each CP result in turn with reference to the structural dimensions shown in figure 2. For LHCP incidence, the LHCP reflectance (LL+, blue curve) shows a broad band, as expected due to the range of pitch values found in the chirped upper helicoid. A strong feature spanning the wavelength range 700 nm to 800 nm is attributed to the concentration of lamellar pitch values for which the scaled fit curve shows a chirp from around 230 nm to 210 nm. The reflectance dip centred on 650 nm corresponds to a more rapidly chirped region, with fewer corresponding pitch contributions. Towards the lower end of the upper helicoid, a cluster of pitch values is found that are scaled to around 160 nm. This feature correlates in part to a contribution to the broad reflectance peak that covers the spectral region between 500 nm and 630 nm. However, no lamellar pitch values are found in the upper

helicoid that appear to correspond with the small reflectance peak that is centred on 450 nm. For RHCP incidence upon the dorsal surface, the RHCP reflectance measurement (RR+, the red curve in figure 3*a*) shows broadband reflectance spanning a wavelength range extending from 500 nm into the near-infrared. The origin of this reflectance component is attributed principally to the lower helicoid, and the form of its spectrum is influenced not only by the large range of lamellar pitch values found in the lower helicoid, but also by the wavelength-dependence of the retardation imparted by the unidirectional layer. The requisite reversal of CP handedness occurs preferentially at wavelengths for which the unidirectional layer imparts a retardation that is close to π. Notably, the RR+ spectrum does not extend to as short a wavelength as the LL+ spectrum despite shorter lamellar pitch contributions being found in the lower helicoid than in the upper helicoid. From this observation we infer that the RR+ bandwidth is limited by the specification of the retarder rather than that of the lower helicoid. The weak cross-polarized reflectance shown in figure 3*a* corresponds partly with the Fresnel reflection arising from the overall refractive index step presented by the sample, in which case the reversal of handedness results from the conventional mirror inversion upon reflection.

In order to investigate further the performance of the retarder, reflectance measurements were performed for incidence upon the exposed underside of the lower helicoid. Figure S2 (see electronic supplementary material) shows spectra for a sample of locations on a piece of elytron following removal of the endocuticle. The results for LL+ and RR+ (figures S2*a* and S2*b* respectively) show that for incidence upon the dorsal surface of this sample the main spectral features were still observed. Figures S2*c* and S2*d* show results for LL– and RR– respectively. A typical measurement of the spectra for incidence upon the exocuticle underside is presented in figure 3*b*. In this case, the LL– response (red curve) may be attributed principally to the lower helicoid but now without the influence of the retarder. The very broad spectrum correlates well with the range of lamellar pitch dimensions found in the lower helicoid. This result indicates that the RR+ spectrum is indeed limited by the performance of the retarder. The absence of short-wavelength components from the RR+ spectrum that are present in the LL– spectrum suggests that the unidirectional layer does not reverse the CP handedness at those wavelengths. This conclusion is supported by the RR– spectrum shown in figure 3*b* (blue curve), which arises from the action of the upper helicoid as well that of the retarder. The spectral components at wavelengths shorter than 500 nm that are present in the LL+ spectrum are absent from the RR– spectrum. A mechanism that would prevent this CP handedness reversal by the unidirectional layer is full-wave retardation within that wavelength regime. With this mechanism in mind, we return to the case of incidence upon the dorsal surface to consider the origin of the small feature in the LL+ spectrum that peaks at 450 nm. The evidence suggests a hypothesis in which the incident LHCP radiation propagates through the upper helicoid, as no lamellar pitch contributions corresponding to such short wavelengths can be identified from the micrographic analysis. On passing through the unidirectional layer, the CP handedness switches to RH and then back to LH as near-2π retardation occurs. The light is then reflected by the shortest lamellar periods that are located around half-way through the lower helicoid. Once again LHCP emerges from the return pass through the unidirectional layer and is transmitted back through the upper helicoid. A similar sequence of considerations indicates that a contribution to the cross-polarized reflectance can originate in the lower helicoid at wavelengths for which the retardation is not equal to an integer multiple of π.

Caveney's direct measurements of the dimensions and refractive index of the unidirectional layer yielded the observation of half-wave retardation at a wavelength of 590 nm. That result does not fit well with the measurements of our specimen, as that wavelength is near the lower limit of the RR+ reflectance band, while a wavelength nearer to the centre of the RR+ band is expected. By inspection of our reflectance measurements, we estimate that the retarder acts as a half-wave plate at a wavelength of around 670 nm and that full-wave retardation occurs in the vicinity of 410 nm. This estimate necessitates the presence of some birefringence dispersion (51). Using these estimates, the in-plane birefringence of the microfibril assembly was calculated for each of the two wavelengths using the relation:

$$\Delta n(\lambda) = \frac{\Delta\varphi(\lambda)\,\lambda}{2\pi l}\,, \qquad [2]$$

where $\Delta\varphi(\lambda)$ is the retardation in radians, λ is the free-space wavelength and l is the thickness of the unidirectional layer. These values were applied to the Sellmeier equation of equation [1] for spatial average index to obtain a fit for the wavelength-dependent birefringence that was applied in the model.

The CP reflectance simulations for incidence upon the dorsal surface are shown in figure 3*c*. By comparison with the corresponding experimental result (figure 3*a*) it is seen that details of the spectra are reproduced, including the main peaks of the LL+ spectrum and short-wavelength limit of the RR+ response. The simulations for incidence on the elytral exocuticle underside surface (figure 3*d*) may be compared with the experimental result (figure 3*b*). The extended spectrum of the LL– response is replicated in the model, while the absence of short wavelengths from the RR– spectrum is also shown.

In assessing the quantitative match between the simulations and the experimental results, certain comparisons are noted. The measurements indicate that a more thorough treatment of the attenuation may be sought, with the suggestion of a larger extinction coefficient at the shorter wavelengths. However, such a trend is not found in the Vargas *et al*. (45) data for chitin and uric acid, which also feature a smaller extinction coefficient than the value chosen. In the simulations, the spectral features generally appear at wavelengths that are some 20 nm to 30 nm shorter than those measured. Such a discrepancy is not unexpected in view of the observed natural variation within the specimen and the scope for uncertainties in the material parameters assigned to the representative structure that was modelled. In the context of the assessment of the applicability of the refractive index data employed, the simulations offer a comparison that highlights the importance of the inclusion of dispersion.

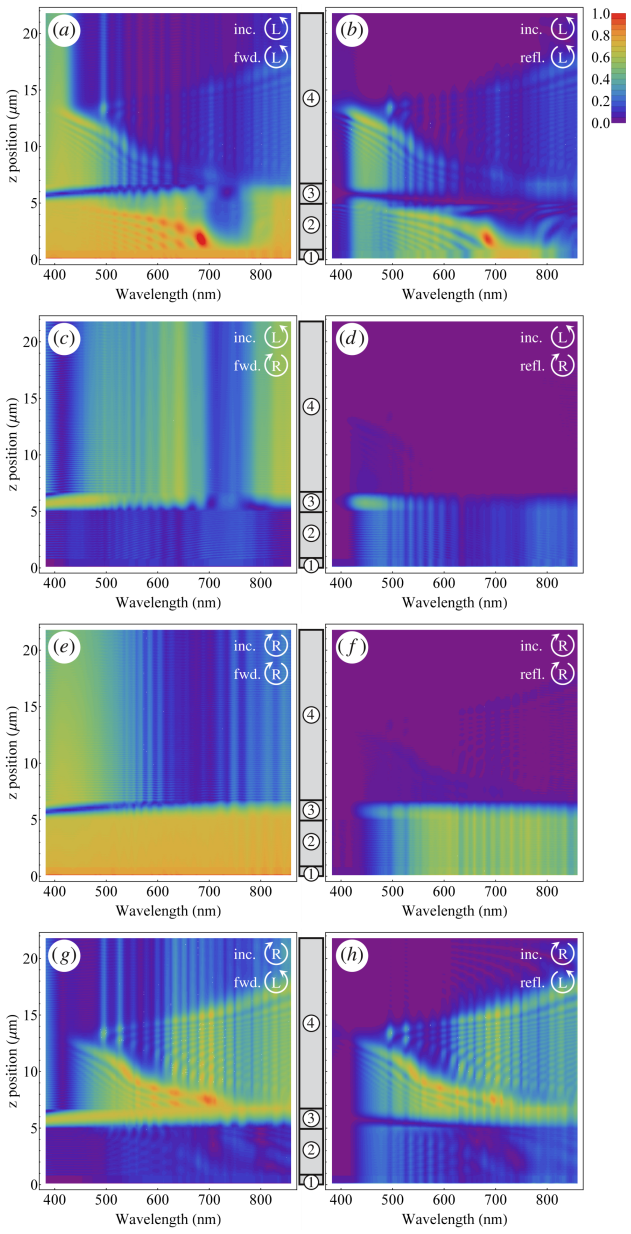

Figure 4. Simulations of CP electric field amplitudes within the reflecting structure for normal incidence upon the dorsal surface of the elytron, decomposed into forward-propagating and backward-propagating (reflected) components. Data are presented for depth *z* through the elytron versus wavelength:
(*a*) to (*d*) LHCP incident field:
(*a*) Forward-propagating LHCP; (*b*) Reflected LHCP;
(*c*) Forward-propagating RHCP; (*d*) Reflected RHCP;
(*e*) to (*h*) RHCP incident field:
(*e*) Forward-propagating RHCP; (*f*) Reflected RHCP;
(*g*) Forward-propagating LHCP; (*h*) Reflected LHCP.
The extent of each region of the structure in the *z* direction is indicated by the vertical bars: 1: epicuticle; 2: upper helicoid; 3: birefringent retarder; 4: lower helicoid. CP handedness is labelled on the plots for incident (inc.) field and either forward-propagating (fwd.) or reflected (refl.) fields. Air is specified as the input medium.

While considering the optical function of helicoids, it is noted that a description of the origin of the CP reflectance and the required conditions for periodicity and helicity may be found in the work of de Vries (20) on cholesteric liquid crystals. A succinct explanation of the preservation of CP handedness on reflection is provided by considering the reflection of a wave at the boundary between two anisotropic sub-layers, whereby both linear components of the wave in the first layer encounter a change of refractive index at the rotated second layer. The fast wave encounters a positive index step that generates a reflected component with inverted phase, while the slow wave is partially reflected without phase reversal. At normal incidence, a mirror applies equal phase shifts to the two components, resulting in the reversal of CP handedness due to the mirror inversion. In the helicoid however, the phase mismatch imparted at the anisotropic interface allows the preservation of the CP handedness upon reflection.

In order to elaborate on the hypothesis described above for the optical function of each component part of the *C. resplendens* multilayer, simulations of the CP field amplitudes within the structure are shown in figure 4. The approach taken is to extract the CP constituents of the fields in the form of forward-propagating and backward-propagating (reflected) components, for normal incidence upon the dorsal surface of the elytron. The data contours are plotted for depth *z* through the structure (ordinate) and wavelength (abscissa). The sections of the vertical bars indicate the *z*-positions of the epicuticle, upper helicoid, unidirectional layer and lower helicoid, labelled 1 to 4 respectively. Figures 4*a* and 4*b* show the forward and reflected LHCP respectively, for an LHCP incident field. The *z* position at which the depletion of the incident field occurs corresponds to the generation of the reflected field. This *z*-dependence may be correlated with details of the helicoidal pitch distribution. For example, LHCP depletion occurs first in the wavelength range 700 nm to 800 nm, corresponding to the longer helicoidal periods that are located near the top of the upper helicoid. Shorter wavelengths are depleted progressively deeper into the upper helicoid since the helicoid is chirped to shorter periods. Most of the residual forward-propagating LHCP is converted to RHCP by the near-half-wave retardation of the unidirectional layer, which is demonstrated in figure 4*c* by the appearance of the forward-propagating RHCP field at $z \approx 6$ μm. This RHCP field propagates through the lower left-handed helicoid with little attenuation. Figure 4*a* also shows the propagation of LHCP wavelengths shorter than 500 nm into the lower helicoid. The presence of this field can be attributed to the absence of corresponding helicoid pitch constituents in the upper helicoid and by the retardation, in region 3, being close to full wave. The dark band that appears at $z \approx 6$ μm has a complementary bright band in figure 4*c*, indicating the conversion to RHCP and back to LHCP. These wavelengths are reflected at a depth of 13 μm to 14 μm in the lower helicoid, where corresponding helicoid pitch constituents are located. Figure 4*d* confirms that very little RHCP is reflected for an LHCP incident field, in contrast to the reflectance of a plane mirror.

The simulations for an RHCP incident field are presented in figures 4*e* to 4*h*. The origin of the RHCP reflectance may be understood by considering these plots in a particular order, as follows. The incident RHCP field propagates forwards (figure 4*e*) through the left-handed upper helicoid, and is converted to contain an LHCP component by the unidirectional layer, subject to the wavelength dependence of its retardation. This conversion occurs most efficiently at a wavelength of 670 nm, at which half-wave retardation is imposed. The strong LHCP field appears in figure 4*g* after the retarder, and is depleted by reflection in the lower helicoid. The

corresponding backward-propagating LHCP field is shown in figure 4*h*. Finally, figure 4*f* shows the generation of the backward-propagating RHCP field in the retarder. This field propagates unopposed back through the upper helicoid. The RHCP reflectance is also affected by both the wavelength dependence of the retardation and the pitch distribution of the lower helicoid.

In conclusion, this study offers evidence to support a new level of detail in the description of the origin of the colour, appearance and optical signature of the beetle *C. resplendens*. Its elytral chiral multilayer configuration performs a sequence of optical functions that achieve broadband, optically-ambidextrous circular polarization reflectance. An additional insight is gained into the level of complexity and optimisation of the mechanism that has evolved to generate these optical properties. The understanding of these functions has the potential to inform the fabrication of novel synthetic optical surfaces for practical applications. This work complements research into the possible behavioural role (52-54) of the conspicuous appearance and circular polarization signature of these insects.

Data accessibility. Relevant experimental data are available online in the supplementary material.

Authors' contributions. All authors contributed to the design of the study, the structural analysis and the interpretation of results; E.D.F. and L.T.M. performed optical experiments and simulations; P.V. coordinated the study; E.D.F. and P.V. drafted the manuscript. All authors gave final approval for publication.

Competing interests. We declare no competing interests.

Funding. This work was supported by AFOSR grant number FA9550-10-1-0020.

Acknowledgements. The authors would like to thank Peter Splatt for microtomy and assistance with the TEM studies, and Dr Simon Horsley for useful discussions.

References

1. Pye JD. 2010 The distribution of circularly polarized light reflection in the Scarabaeoidea (Coleoptera). *Biol. J. Linn. Soc*. **100**, 585-596. (doi: 10.1111/j.1095-8312.2010.01449.x)
2. Gaubert P. 1924 Sur la polarisation circulaire de la lumière réfléchie par les Insectes. *Comptes Rendus* **179**, 1148-1150.
3. Mathieu JP, Faraggi N. 1937 Étude de la lumière polarisée circulairement réfléchie par certains Coléoptères. *Comptes Rendus* **205**, 1378-1380.
4. Arwin H, Magnusson R, Landin J, Järrendahl K. 2012 Chirality-induced polarization effects in the cuticle of scarab beetles: 100 years after Michelson. *Phil. Mag.* **92**, 1583-1599. (doi:10.1080/14786435.2011.648228)
5. Seago AE, Brady P, Vigneron J-P, Schultz TD. 2009 Gold bugs and beyond: A review of iridescence and structural colour mechanisms in beetles (Coleoptera) *J. R. Soc. Interface* **6**(Suppl 2), S165–S184. (doi:10.1098/rsif.2008.0354.focus)
6. Boucard A. 1875 Monographic List of the Coleoptera of the Genus *Plusiotis* of America, north of Panama, with Descriptions of several new Species. *Proc. Zool. Soc. Lond.* **1875**, 117-125.
7. Michelson AA. 1911 On metallic colouring in birds and insects. *Phil. Mag*. **21**, 554-567. (doi:10.1080/14786440408637061)
8. Caveney S. 1971 Cuticle reflectivity and optical activity in scarab beetles: the role of uric acid. *Proc. R. Soc. Lond. B* **178**, 205–225. (doi:10.1098/rspb.1971.0062)
9. Neville AC, Caveney S. 1969 Scarabeid beetle exocuticle as an optical analogue of cholesteric liquid crystals. *Biol. Rev.* **44**, 531–562. (doi:10.1111/j.1469-185X.1969.tb00611.x)
10. Neville AC, Luke BM. 1969 A Two-System Model for Chitin-Protein Complexes in Insect Cuticles. *Tissue & Cell* **1**, 698-707. (doi:10.1016/S0040-8166(69)80041-8)
11. Bouligand Y. 1965 Sur une architecture torsadée répandue dans la nombreuses cuticules d'Arthropodes. *C. R. Hebd. Séances Acad. Sci. Paris* **26**, 3665–3668.
12. Neville AC. 1993 Biology of Fibrous Composites: *Developments Beyond the Cell Membrane* (Cambridge Univ Press, UK), pp 85–123.
13. Wilts BD, Whitney HM, Glover BJ, Steiner U, Vignolini S. 2014 Natural helicoidal structures: morphology, self-assembly and optical properties. *Mater. Today: Proc.* **1S**, 177-185. (doi:10.1016/j.matpr.2014.09.021)
14. Vignolini S, Rudall PJ, Rowland AV, Reed A, Moyroud E, Faden RB, Baumberg JJ, Glover BJ, Steiner U. 2012 Pointillist structural color in *Pollia* fruit. *Proc. Natl. Acad. Sci. USA* **109**, 15712–15715. (doi:10.1073/pnas.1210105109)
15. Vignolini S, Gregory T, Kolle M, Lethbridge A, Moyroud E, Steiner U, Glover BJ, Vukusic P, Rudall PJ. 2016 Structural colour from helicoidal cell-wall architecture in fruits of *Margaritaria nobilis. J. R. Soc. Interface* **13**, 20160645. (doi:10.1098/rsif.2016.0645)
16. Gould KS, Lee DW. 1996 Physical and Ultrastructural Basis of Blue Leaf Iridescence in Four Malaysian Understory Plants. *Am. J. Bot.* **83**, 45-50.
17. Neville AC, Levy S. 1984 Helicoidal orientation of cellulose microfibrils in *Nitella opaca* internode cells: ultrastructure and computed theoretical effects of strain reorientation during wall growth. *Planta* **162**, 370-384. (doi:10.1007/BF00396750)
18. Giraud-Guille M-M, Bessau L, Martin R. 2003 Liquid crystalline assemblies of collagen in bone and in vitro systems. *J. Biomech*. **36**, 1571-1579. (doi:10.1016/S0021-9290(03)00134-9)
19. Bessau L, Bouligand Y. 1998 The twisted collagen network of the box-fish scutes. *Tissue & Cell* **30**, 251-260. (doi:10.1016/S0040-8166(98)80073-6)
20. de Vries H. 1951 Rotatory Power and Other Optical Properties of Certain Liquid Crystals, *Acta Cryst.* **4**, 219-226. (doi: 10.1107/S0365110X51000751)
21. Chiou T-H, Kleinlogel S, Cronin T, Caldwell R, Loeffler B, Siddiqi A, Goldizen A, Marshall J. 2008 Circular polarization vision in a stomatopod crustacean. *Curr. Biol*. **18**, 429–34. (doi:10.1016/j.cub.2008.02.066)
22. Roberts NW, Chiou T-H, Marshall NJ, Cronin TW. 2009 A biological quarter-wave retarder with excellent achromaticity in the visible wavelength region. *Nat. Photon*. **3**, 641-644. (doi:10.1038/nphoton.2009.189)
23. Jewell SA, Vukusic P, Roberts NW. 2007 Circularly polarized colour reflection from helicoidal structures in the beetle *Plusiotis boucardi*. *New J. Phys*. **9**, 99. (doi: 10.1364/OPN.18.12.000033)
24. Goldstein DH. 2006 Polarization properties of Scarabaeidae. *Appl. Opt*. **45**, 7944–7950. (doi:10.1364/AO.45.007944)
25. Fernández del Río L. 2011 An Investigation of the Polarization States of Light Reflected from Scarab Beetles of the *Chrysina* Genus. *Linköping University Diploma Work*.
26. Hegedüs R, Szél G, Horváth G. 2006 Imaging polarimetry of the circularly polarizing cuticle of scarab beetles (Coleoptera: Rutelidae, Cetoniidae). *Vision Res.* **46**, 2786–2797. (doi:10.1016/j.visres.2006.02.007)
27. Hodgkinson I, Lowrey S, Bourke L, Parker A, McCall MW. 2010 Mueller-matrix characterization of beetle cuticle: polarized and unpolarized reflections from representative architectures. *Appl. Opt.* **49**, 4558-4567. (doi:10.1364/AO.49.004558)
28. Song MH, Park B, Shin K-C, Ohta T, Tsunoda Y, Hoshi H, Takanishi Y, Ishikawa K, Watanabe J, Nishimura S *et al*. 2004 Effect of Phase Retardation on Defect-Mode Lasing in Polymeric Cholesteric Liquid Crystals. *Adv. Mater.* **16**, 779-783. (doi:10.1002/adma.200306360)
29. Hwang J, Song MH, Park B, S. Nishimura S, Toyooka T, Wu TJ, Takanishi Y, Ishikawa K, Takezoe H. 2005 Electro-tuneable optical diode based on photonic bandgap liquid-crystal heterojunctions. *Nat. Mater*. **4**, 383–387. (doi:10.1038/nmat1377)
30. Matranga A, Baig S, Boland J, Newton C, Taphouse T, Wells G, Kitson S. 2013 Biomimetic Reflectors Fabricated Using Self-Organising, Self-Aligning Liquid Crystal Polymers. *Adv. Mater*. **25**, 520-523. (doi:10.1002/adma.201203182)
31. Berreman DW. 1972 Optics in Stratified and Anisotropic Media: 4 X 4-Matrix Formulation. *J. Opt. Soc. Am*. **62**, 502-510. (doi:10.1364/JOSA.62.000502)
32. Yeh P. 1979 Electromagnetic propagation in birefringent layered media. *J. Opt. Soc. Am*. **69**, 742-756. (doi:10.1364/JOSA.69.000742)
33. Lin-Chung PJ, Teitler S. 1984 4 X 4 Matrix formalisms for optics in stratified anisotropic media. *J. Opt. Soc. Am. A* **1**, 703-705. (doi:10.1364/JOSAA.1.000703)
34. Ko DYK, Sambles JR. 1988 Scattering matrix method for propagation in stratified media: attenuated total reflection studies of liquid crystals. *J. Opt. Soc. Am. A* **5**, 1863–1866. (doi:10.1364/JOSAA.5.001863)
35. Weis-Fogh T. 1970 Structure and Formation of Insect Cuticle. *Symp. R. Ent. Soc. Lond. 5: Insect Ultrastructure*, ed Neville AC. Blackwell Scientific Publications, UK), pp 165-185.
36. Lockey KH. 1988 *Lipids of the Insect Cuticle: Origin, Composition and Function. Comp. Biochem. Physiol.* **89B**, 595-645. (doi:10.1016/0305-0491(88)90305-7)
37. Lenau T, Barfoed M. 2009 Colours and Metallic Sheen in Beetle Shells—A Biomimetic Search for Material Structuring Principles Causing Light Interference. *Adv. Eng. Mat.* **10**, 299-314. (doi:10.1002/adem.200700346)
38. Bouligand Y. 1986 Theory of Microtomy Artefacts in Arthropod Cuticle. *Tissue & Cell* **18**, 621-643. (doi:10.1016/0040-8166(86)90025-X)
39. Crang RFE, Klomparens KL (eds.). 1988 *Artifacts in Biological Electron Microscopy*, Plenum Press, New York.
40. Parker AR, McKenzie DR, Large MCJ. 1998 Multilayer reflectors in animals using green and gold beetles as examples. *J. Exp. Biol*. **201**, 1307-1313.

41. Noyes JA, Vukusic P, Hooper IR. 2007 Experimental method for reliably establishing the refractive index of buprestid beetle exocuticle. *Opt. Express* **15**, 4352-4358. (doi:10.1364/OE.15.004351)
42. Yoshioka S, Kinoshita S. 2011 Direct determination of the refractive index of natural multilayer systems. *Phys. Rev. E* **83**, 051917. (doi:10.1103/PhysRevE.83.051917)
43. Shawkey MD, Moorhouse NI, Vukusic P. 2009 A Protean Palette: Colour Materials and Mixing in Birds and Butterflies. *J. R. Soc. Interface* **6**, S221-S231. (doi:10.1098/rsif.2008.0459.focus)
44. Leertouwer HL, Wilts BD, Stavenga DG. 2011 Refractive index and dispersion of butterfly chitin and bird keratin measured by polarizing interference microscopy. *Opt. Express* **19**, 24061. (doi:10.1364/OE.19.024061)
45. Vargas WE, Azofeifa DE, Arguedas HJ. 2013 Índices de refracción de la quitina, el quitosano y el ácido úrico con aplicación en análisis de color estructural. *Óptica Pura y Aplicada* **46**, 55–72. (doi:10.7149/OPA.46.1.55)
46. Libby E, Azofeifa DE, Hernández-Jiménez M, Barboza-Aguilar C, Solís A, García-Aguilar I, Arce-Marenco L, Hernández A, Vargas WE. 2014 Light reflection by the cuticle of *C. aurigans* scarabs: a biological broadband reflector of left handed circularly polarized light. *J. Opt.* **45**(082001), 1–7. (doi:10.1088/2040-8978/16/8/082001)
47. Bruggeman DAG. 1935 Berechnung verschiedener physikalischer Konstanten von heterogenen Substanzen. I. Dielektrizitatskonstanten und Leitfahigkeiten der Mischkorper aus isotropen Substanzen. *Ann. Phys.* **24**, 636-664. (doi:10.1002/andp.19354160705)
48. Vukusic P, Sambles JR, Lawrence CR, Wootton RJ. 1999 Quantified interference and diffraction in single *Morpho* butterfly scales. *Proc. R. Soc. Lond. B* **266**, 1403-1411. (doi: 10.1098/rspb.1999.0794)
49. Stavenga DG, Leertouwer HL, Wilts BD. 2013 Quantifying the refractive index dispersion of a pigmented biological tissue using Jamin–Lebedeff interference microscopy. *Light Sci. Appl.* **2**:e100. (doi:10.1038/lsa.2013.56)
50. Hooper IR, Vukusic P, Wootton RJ. 2006 Detailed optical study of the transparent wing membranes of the dragonfly *Aeshna cyanea*. *Opt. Express* **14** 4891-4897. (doi: 10.1364/OE.14.004891)
51. Ghosh G. 1999 Dispersion-equation coefficients for the refractive index and birefringence of calcite and quartz crystals. *Opt. Comm*. **163**, 95-102. (doi:10.1016/S0030-4018(99)00091-7)
52. Brady P, Cummings M. 2010 Differential Response to Circularly Polarized Light by the Jewel Scarab Beetle *Chrysina gloriosa*. *Am. Nat*. **175**, 614–20.
53. Blahó M, Egri Á, Hegedüs R, Jósvai J, Tóth M, Kertész K, Biró LP, Kriska G, Horváth G. 2012 No evidence for behavioral responses to circularly polarized light in four scarab beetle species with circularly polarizing exocuticle. *Physiol. & behav.* **105**, 1067-1075. (doi:10.1016/j.physbeh. 2011.11.020)
54. Miao J, Wu Y-Q, L K-B, Jiang Y-L, Gong Z-J, Duan Y, Li T. 2015 Evidence for Visually Mediated Copulation Frequency in the Scarab Beetle *Anomala corpulenta. J. Insect. Behav.* **28**, 175–182. (doi: 10.1007/s10905-015-9487-3)